

We are IntechOpen, the world's leading publisher of Open Access books Built by scientists, for scientists

5,500

Open access books available

136,000

International authors and editors

170M

Downloads

Our authors are among the

154

Countries delivered to

TOP 1%

most cited scientists

12.2%

Contributors from top 500 universities



WEB OF SCIENCE™

Selection of our books indexed in the Book Citation Index
in Web of Science™ Core Collection (BKCI)

Interested in publishing with us?
Contact book.department@intechopen.com

Numbers displayed above are based on latest data collected.
For more information visit www.intechopen.com



Raman Spectroscopy and Mapping Analysis of Low-Dimensional Nanostructured Materials and Systems

Karthikeyan Krishnamoorthy and Sang-Jae Kim

Abstract

This chapter describes the use of Raman spectroscopy and mapping analysis for the characterization of low dimensional nanostructures, including 2D sheets (graphene oxide, graphene sheets, MoS₂, siloxene), and one-dimensional carbyne chains. The Raman mapping analysis and their application towards understanding the molecular level interactions in these low dimensional materials, nanostructured polymer composites, and nanopaints are also discussed. The stoichiometric composition and structure of these low dimensional materials were correlated with the Raman spectral and mapping analysis. Further, Raman spectroscopy for understanding or probing the mechanism of mechanical to electrical energy harvesting properties of carbyne films via the structural transformation from cumulene to polynne networks of carbyne is demonstrated.

Keywords: Raman spectroscopy, Raman mapping, graphene oxide, graphene, MoS₂, siloxene, carbyne, nanocomposites

1. Introduction

Raman spectroscopy is a promising non-destructive testing of materials to understand their crystallinity, chemical bonding vibrations and effects of surface defects [1, 2]. The Raman spectroscopy becomes an important technique for the characterization of nanostructured materials, especially the two-dimensional (2D) materials (such as graphene, MoS₂, siloxene, metalenes), biomaterials, composites, and for understanding energy-conversion process in the recent years [3–5]. Additionally, these techniques are useful for criminological & forensic applications, biomedical applications, and as well as bio-sensors for health care sectors [6–8]. The basic principle of Raman spectroscopy relies on the “Raman effect”, i.e., the inelastic scattering of light which can directly probe vibration and rotational-vibration states of any molecules and/or materials [9]. In 1923, Smekal et al. predicted the Raman scattering of light using molecules explained via classical quantum theory which was experimentally observed by Raman and Krishnan in 1928 [10]. Based on this principle, nearly 25 types of Raman spectroscopic techniques are available for characterization of different materials for various applications. Some of them are (i) spontaneous Raman, (ii) hyper-Raman scattering, (iii) Fourier-transform

Raman scattering, (iv) Raman-induced Kerr-effect spectroscopy and (v) stimulated-coherent Raman and so on [9]. There are numerous works discussed the fundamental principles and theory of Raman spectroscopy and their working mechanism were available in literature [11, 12]. In addition to these, Raman mapping is often used for identification of various information such as crystallinity, homogeneity, defect sites and molecular level bonding for materials science research [13, 14]. This book chapter focus on the use of Raman spectroscopy and mapping analysis for studying the molecular level vibrations in the 2D materials, composites, solid electrolyte entrapped in piezo-polymer matrix, low-dimensional materials such as carbyne chains, and probing method for elucidating the mechanism of energy harvesting in carbyne via mechanical stimuli.

2. Experimental section

2.1 Preparation of graphene oxide with different oxidation levels, graphene sheets and graphene nanopaint

The modified Hummers method is used for the preparation of graphene oxide sheets using the chemical reaction between graphite powders with potassium permanganate, and sulfuric acid. The oxidation degree of graphene oxide was varied via changing the concentration of potassium permanganate by keeping the remaining parameters constant as reported in our earlier work [15]. The graphene sheets were prepared via the reduction of graphene oxide using hydrazine hydrate in presence of ultrasound irradiation [16]. The graphene based nanopaint was obtained by mechanical milling process for 12 h using appropriate amount of graphene sheets (pigment) and alkyd resin binder. The graphene paint was coated on glass substrate using brush coating [17].

2.2 Preparation of 2D molybdenum disulphide nanosheets and quantum sheets

A hydrothermal method is used for the formation of MoS₂ on the surface of Mo foil (Mo source) using thiourea (sulfur source). The hydrothermal reaction process is carried out for 24 h at a temperature of 180 °C. The detailed experimental procedure can be seen from our reported work [18].

2.3 Preparation of 2D siloxene sheets

The siloxene nanosheets was obtained via topochemical de-intercalation reaction between calcium disilicide and conc. Hydrochloric acid at a temperature of 0 °C for four days [19].

2.4 Preparation of 2D antimonene

The 2D antimonene with nanodendrites structures anchored on the surface of the Ni foam was achieved via a facile electrochemical deposition process as mentioned in literature [20].

2.5 Preparation of proton conducting solid electrolyte-piezoelectric PVDF hybrids

The piezo-polymer electrolyte nanocomposite film made of phosphotungstic acid (PTA) solid electrolyte and PVDF were obtained by ultrasound irradiation

followed by solvent casting method [16]. Appropriate amount of PVDF was dissolved in dimethylacetamide and acetone with the use of ultrasonication in which different weight ratios (5–25 wt%) of PTA electrolyte was added under mechanical stirring and ultrasound irradiation process. Then, the entire solution was transferred into a Petri dish and allowed to dry at 70 °C for complete evaporation of the solvents which led to the formation of PTA-PVDF piezo-electrolyte film via peel-off process.

2.6 Preparation of free standing carbyne-enriched carbon (CEC) films

The CEC film was prepared by immersing the free-standing PVDF film in a solution containing dehydrohalogenation mixture (potassium ethylate and tetrahydrofuran) in presence of ultrasound irradiation for 2 h [21, 22]. The change in color from white (PVDF) into black (CEC) confirms the occurrence of dehydrohalogenation process. Then, the CEC film was rinsed with ethanol to removal chemical impurities and dried at 60 °C. The entire reaction was performed inside an Ar-filled glove box.

2.7 Raman spectral and mapping acquisition

The Raman spectral and mapping acquisition of the samples were carried out on a LabRam HR-Evolution Raman spectrometer (Horiba Jobin-Yvon, France). The Raman system used an Ar⁺ ion laser operating at a laser power of 15 mW with an excitation wavelength of 514 nm. The Raman mapping of samples were performed over the desired area to obtain spectral arrays. The results are processed and analyzed using software. The spectral arrays map was processed and analyzed using classical least squares (CLS) fitting (multivariate analysis) method on LabSpec (Ver. 6.2) software.

3. Results and discussion

3.1 Raman spectral studies of graphene oxide with various levels of oxidation

This section focused on the use of Raman spectroscopy as a promising tool for characterizing graphene-based materials and their system. It is well known that graphene sheets emerged as a material of this decade due to their wide-spread properties and applications in variety of sectors [23]. For preparation of gram-scale graphene sheets, researchers often used graphitic oxide or graphene oxide as a starting material that is originally synthesized a century ago [24]. Graphene is a one-atom thick sheet in which hexagonal carbon chains are present laterally [25]. The structure of graphene oxide is similar to that of graphene in which the carbon atoms are bonded with different functional groups (hydroxyl, carbonyl, carboxyl, and epoxide) [26]. The formation of these groups occurred because of oxidation of graphite and removal of these groups lead to the formation of chemically derived graphenes.

In general, the Raman spectrum of graphite possess G band (first order scattering of the E_{2g} mode), D band cm^{-1} (defects), and 2D band (c-axis stacking order) at 1570, 1354, and 2700 cm^{-1} , respectively [1]. **Figure 1(A)** shows the Raman spectra of graphene oxide sheets with different oxidation degrees (S1-S6 shows the low to high oxidation content). It shows that the increase in oxidation degree results in the shift of G band position (in comparison with graphite) towards higher wavenumber and reaches to 1596 cm^{-1} for the heavily oxidized graphene

oxide (**Figure 1(B)**) [15]. The full-width half maximum (FWHM) of the G band raised from 45 to 124 cm^{-1} with increase in oxidation level (**Figure 1(B)**). The shift in G band position and increase in FWHM is due to the formation of different levels of sp^3 hybridized carbons with respect to the oxidation process. Likewise, the D band in graphene oxide is broadened (increased FWHM) and highly intense in comparison with graphite, i.e., due to the formation more defects and disorders as a result of oxidation process [27]. The intensity of the 2D band reduces after oxidation process because of breaking of stacking order and new band is observed around 2950 cm^{-1} that is denoted as D + G band. At much higher oxidation levels, the peak broadening of 2D band is observed. **Figure 1(C)** shows the plot of $I_{(D)}/I_{(G)}$ and $I_{(2D)}/I_{(G)}$ ratio versus the oxidation degree of graphene oxide. The $I_{(D)}/I_{(G)}$ ratio rises with initial increase in oxidation and decreased/saturated at higher degrees that is compensated by the higher FWHM. The variation of $I_{(2D)}/I_{(G)}$ ratio (**Figure 1(C)**) against the oxidation degree of graphene oxide indicating that they tend to decrease up to S-3 and increases at higher oxidation levels. These changes indicated the decrease in crystallinity and increase in amorphous nature in graphene oxide with increase in oxidation ranges. Further, the observed changes in overtone bands (2D, D + G and 2G), confirms the disruption of the stacking order in graphene oxide at higher oxidation level. The average crystallite size (L_a) of the sp^2 domains present in the prepared graphene oxides was determined in accordance with the method given by Cancodo et al. [28]. The L_a values are 18.2, 11.2, 9.6, 15.6, 14.0, and 13.7 nm for the different graphene oxides (from S-1 to S-6), and these values are lesser than the L_a of graphite (122 nm). These results indicated that there is no linear relation to quantify the amounts of sp^3 and sp^2 domains present in graphene oxide with different oxidation degrees. Altogether, the Raman analysis showed the occurrence crystalline to amorphous transition with disruption of stacking order when graphite is oxidized into graphene oxide.

3.2 Raman spectral and mapping studies on graphene-based nanopaint

This section describes the use of Raman mapping for the identification of pigment dispersion in alkyd resin-based paint coating which utilizes graphene sheets as pigment and/or conductive agent. These electrically conductive paints are

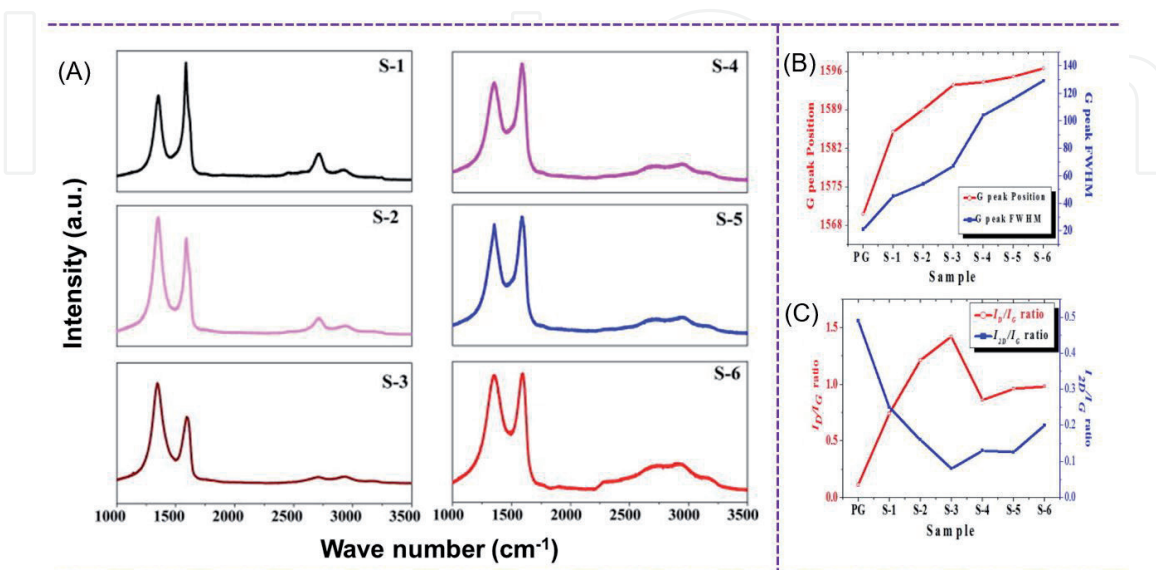


Figure 1. (A) Raman spectra of graphene oxide with different oxidation level, (B) variation of G peak position and full width half maximum ratio with respect to the oxidation degree of graphene oxide, (C) plot of (B) $I_{(D)}/I_{(G)}$ and $I_{(2D)}/I_{(G)}$ ratio versus the oxidation degree of graphene oxide.

of high significance with applications ranging from electromagnetic interference shielding, static charge dissipation, and space [29, 30]. The comparative Raman spectrum of graphene paint and alkyd resin is given in **Figure 2(A)**. The spectrum of graphene paint coatings indicating the presence of G band (1585 cm^{-1}), and D band (1350 cm^{-1}) which confirms the presence of graphene sheets dispersed well in the alkyd resin binder [31, 32]. There were no bands related to the alkyd resin were observed in the Raman spectrum of graphene paint coating since the vibrations arise from graphene sheets overwhelms the vibrations of alkyd resin. The peak position and intensity ratios of finger imprint modes were used to study the spatial distribution of graphene sheets in the paint matrix. **Figure 2(B)–(D)** presents the peak position maps of graphene's finger imprint bands such as D band ($1350\text{--}1370\text{ cm}^{-1}$), G band ($1584\text{--}1590\text{ cm}^{-1}$) and 2D band ($2710\text{ to }2730\text{ cm}^{-1}$), respectively. In comparison with the Raman spectrum of bare graphene sheets alone, the G band is red shifted as a result of molecular level bonding between the graphene sheets with the functional groups of alkyd resin [17]. Additionally, G and 2D bands of graphene sheets were seen over the entire mapped regime of the paint coatings that is responsible for the observed electrical conductivity. **Figure 2(E)** shows the intensity ratio map of I_D/I_G band in the range from 0.20 to 0.55 (blue to yellow) revealed the interconnection between of sp^2 domains of graphene with alkyd resin counterparts in the prepared paint coating. The I_{2D}/I_G ratio map (**Figure 2(F)**) is from of 0.25 to 0.65 (blue to yellow) indicating the restacking of graphene sheets (c-axis) occurred in the paint coating. This uniform distribution of restacked graphene sheets inside the alkyd resin matrix provides enough conductive channels to facilitate the electrical transport in the graphene paint [17].

3.3 Raman analysis of 2D materials directly grown on conductive substrate

In this section, we discuss about the use of Raman spectroscopy as a prominent tool understanding the crystallinity and layer numbers of 2D materials that are randomly or vertically oriented on the conductive substrates. Generally, binder-free electrodes neglecting the inclusion of insulating polymers are of great significance in electrochemical energy conversion and storage devices since they offer enhanced

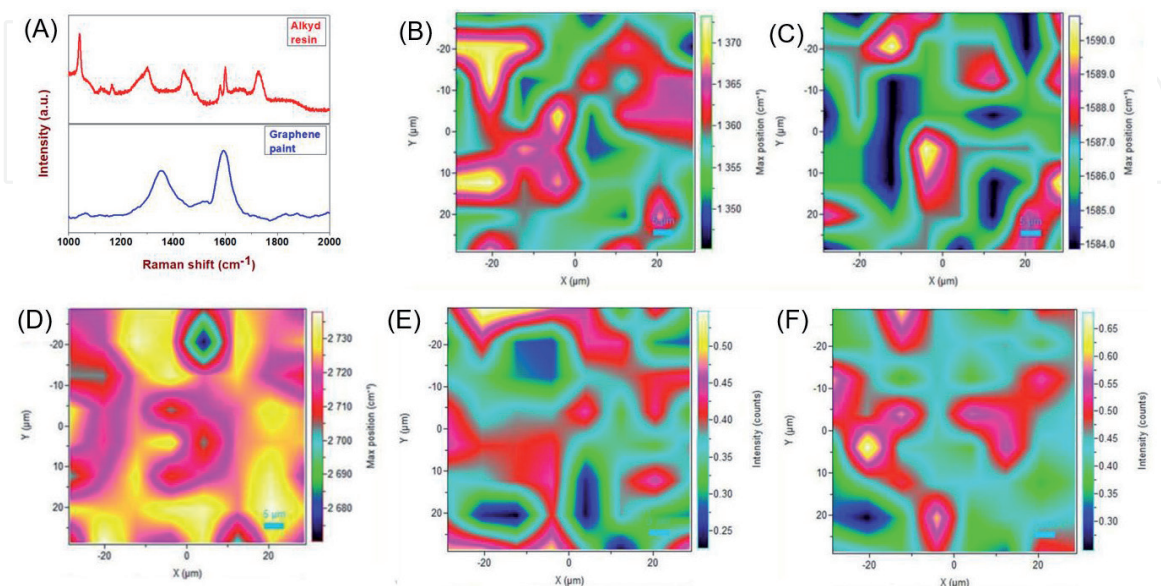


Figure 2. Raman characterization of graphene paint coatings. (A) Raman spectrum of graphene paint in comparison with alkyd resin, peak position maps of (B) D, (C) G, and (D) 2D bands, respectively. Intensity ratio maps of (E) I_D/I_G and (F) I_{2D}/I_G bands, respectively.

electrochemical active sites [33, 34]. Usually, atomic force microscope (AFM) is used for the understanding the thickness of the 2D sheets whereas this technique is suitable only for laterally oriented sheets [35]. The AFM technique is not suitable for measurements for samples such as randomly or vertically aligned sheets on conductive substrates due to the structural issues [18]. Herein, Raman spectroscopy and mapping analysis are promising for these types of binder-free electrodes that are mainly used in electrochemical energy devices.

In recent years, MoS₂ sheets are considered as structural analogue to graphene due to their structural integrity in which the covalently bonded S-Mo-S layers were separated by Van der Waals forces [36]. These layered structure and redox properties of Mo transition metal led to superior electrochemical charge-storage properties (supercapacitors) which is extensively studied during this decade [37]. Additionally, the presence of band gap in MoS₂ that make them as an ideal candidate for optoelectronic, field effect transistor, and photoelectrochemical cells [38]. The specific capacitance of MoS₂ electrode fabricated using conventional slurry coating method is in the range of 80 to 120 F g⁻¹ [39]. To boost the specific capacitance, binder-free MoS₂ electrodes were fabricated via growing MoS₂ directly on conductive substrates such as Mo foil, and Ni foam. Interestingly, the specific capacitance of MoS₂/Mo foil increases upto 192 F g⁻¹ that is higher compared to many of the reported MoS₂ based planar supercapacitor electrodes and these electrodes possess better Columbic efficiency than others [18]. To understand the structural properties of MoS₂/Mo binder-free electrodes, Raman mapping analysis were performed. **Figure 3(A)** shows the Raman spectrum of MoS₂ sheets randomly aligned on Mo foil. The presence of Raman fingerprint bands of MoS₂ at 381 cm⁻¹ (E_{2g}¹ mode) and 405 cm⁻¹ (A_{1g} mode) is observed in **Figure 3(A)**. The intensity ratio between these bands, and their band positions can be directly correlated to their thickness [40]. **Figure 3(B)** shows the integral intensity ratio map of E_{2g}¹/A_{1g} modes shows that their ratio varies from 0.1 to 0.7. Bulk MoS₂ possess an intensity ratio of 0.7 whereas tri-, bi-, and mono-layered MoS₂ have an intensity ratio of 0.6, 0.3 and 0.1 based on previous works [41]. Therefore, **Figure 3(B)** confirms the presence of minor fractions with single-layer MoS₂ (blue color), major fractions with bi-layered MoS₂ (green color), few layered (n < 6) MoS₂ (red color) and some bulk counterparts (yellow color) present in the MoS₂/Mo foil [18]. **Figure 3(C)** and **(D)** shows the peak position maps of A_{1g} and E_{2g}¹ modes which shows their variation from 403 to 410 cm⁻¹ (bulk to single-layer) and from 380 to 386 cm⁻¹ (bulk to single-layer), respectively [18]. The presence of bulk and few-layered MoS₂ is due to the initial phase of the reaction due to Kirkendall effect and secondary phase resulting in the randomly oriented sheets. Altogether, the Raman mapping analysis confirmed the presence of few-layered MoS₂ sheets (n < 5) and some bulk counterparts were grown on the Mo foil.

Likewise, in our recent study, Raman spectroscopy coupled with mapping is effectively used to quantify the thickness of the antimonene nanodendrites grown on the surface of nickel foam via electrochemical deposition technique [20]. Antimonene is one of the important materials from the family of 2D metalenes (P, Sb, As, and Bi) due to their semi-metallic properties [42], high carrier mobility [43], oxidation resistant nature, and tuneable band gap that make them as alternative candidate for application in solar cells [44], CO₂ reduction [45], biological applications, supercapacitors, and batteries [20, 46]. Usually, antimonene sheets can be prepared via exfoliation methods (mechanical or liquid phase) like other 2D materials, whereas the yield is low. Recently, chemical/physical vapor deposition techniques were used to grow antimonene on conductive substrates [47]. In our

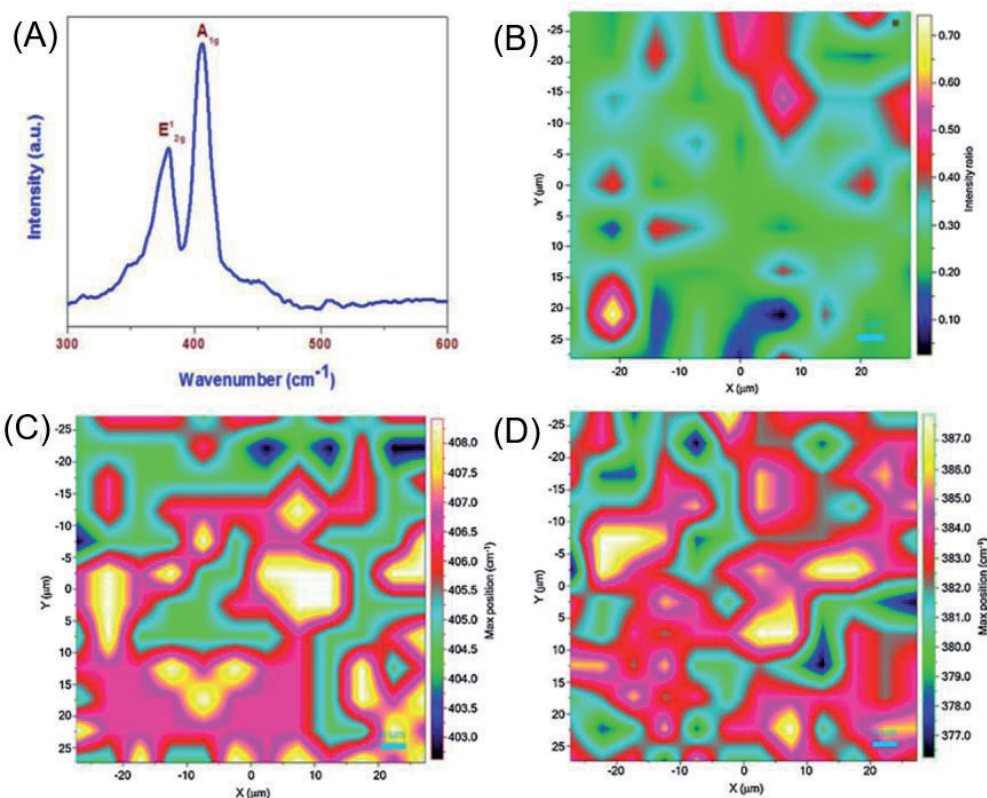


Figure 3. Raman characterization of MoS₂ nanosheets grown on Mo foil. (A) Raman spectrum, (B) E'_{2g}/A_{1g} intensity ratio map, (C) A_{1g} peak position map, and (D) E'_{2g} peak position map.

recent work, we demonstrated the use of electrosynthesis route for the preparation of antimonene nanodendrites grown on nickel foam and these electrodes showed excellent charge-storage properties with a high specific capacity (1618 mA g⁻¹) than of the reported binder-free electrodes [20]. Herein, Raman mapping analysis is used for the identification of layer numbers in antimonene. Based on the E_g/A_{1g} intensity ratio map of antimonene nanodendrites that showed a ratio values vary from 0.41 to 0.49, the presence of few-layered sheets in the prepared antimonene/Ni foam binder-free electrodes were confirmed [48].

3.4 Raman analysis of siloxene sheets

Siloxene sheets are one of the emerging materials from the 2D silicon family that can be prepared via topochemical reaction (given in Section 2.3) between CaSi₂ (Figure 4(A)) with conc. HCl that results in the dissolution of calcium ions and oxidation of Si sheets (Figure 4(B)) [19, 49]. The structure of siloxene consists of Si₆ rings interconnected through Si–O–Si bridges with the addition of surface-terminated hydroxyl groups as seen in Figure 4(C) [19]. Siloxene sheets can be explained as an oxidized form of silicene sheets, and the latter is known for their excellent conductivity comparable to that of graphene [50]. Further, the 2D siloxene or silicene sheets are highly useful for micro-electronic devices since existing technology is established based on silicon [19]. Recent studies on siloxene sheets shows that they are promising candidate for applications in water splitting, Li-ion batteries, supercapacitors, electrochemical sensors, and biomedical fields [51–54]. However, the structure of siloxene is quite complicated and there are different models (such as Weiss structure, chain-like structure, and Kautsky structure) were proposed till date [54]. The Raman spectrum of siloxene sheets (Figure 4(D)) showed the presence of two bands viz. (i) Si–O–Si (495 cm⁻¹) and Si–Si ((520 cm⁻¹)

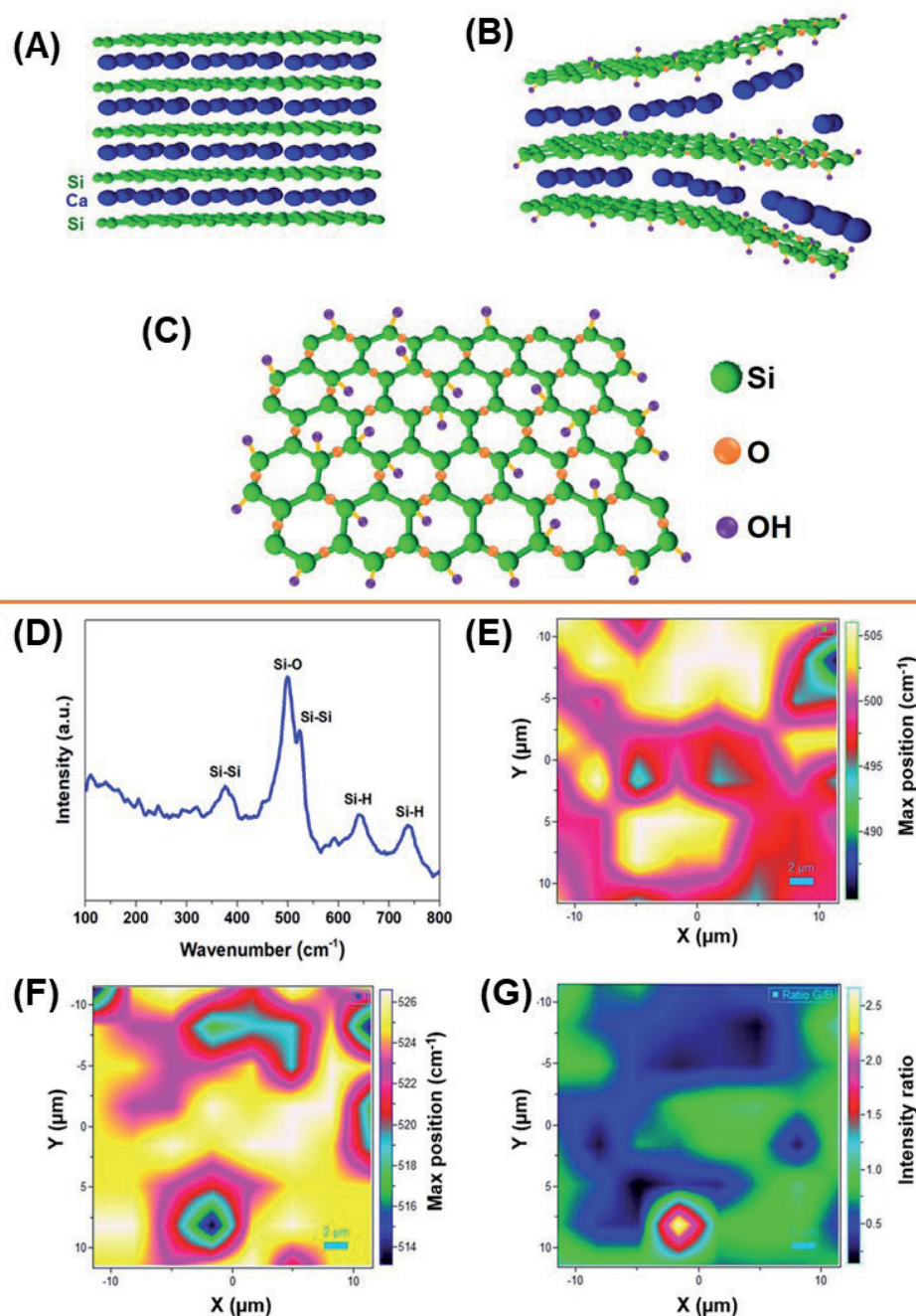


Figure 4. (A) Structure of CaSi_2 , (B) dissolution of Ca from CaSi_2 during the topochemical reaction, (C) structure of siloxene sheets, (D) Raman spectrum of siloxene sheets, (E-F) peak position maps of (E) Si-O-Si and (F) Si-Si, and (G) intensity ratio map of $I_{(\text{Si-O-Si})}/I_{(\text{Si-Si})}$. Reproduced from ref. 19 with permission from the Royal Society of Chemistry.

which showed that Kautsky structure of siloxene [52]. The minor bands present at 375 cm^{-1} is due to $\nu_{(\text{Si-Si})}$ and others located at 640 and 740 cm^{-1} are originated from $\nu_{(\text{Si-H})}$. The peak position maps of Si-O-Si and Si-Si (**Figure 4(E)** and (**F**)) vibrations shows that they vary from 495 to 505 cm^{-1} and from 518 to 526 cm^{-1} , respectively. Here, the Si-Si and Si-O-Si bonds relates to the crystalline and amorphous domains of the siloxene sheets [19], and therefore, their intensity ratio map was constructed as shown in **Figure 4(G)**. The intensity ratio map of Si-O-Si/Si-Si bands revealed that they vary from 0.3 to 2.0 over the entire mapped region. This highlighted the heterogenous distribution of Si-O-Si bridged over the Si_6 rings in the structure of siloxene and confirmed the presence of Kautsky structure [55].

3.5 Raman analysis of solid electrolyte-piezopolymer nanocomposite

Polymer electrolyte composites play a key role in a variety of electrochemical energy conversion-, storage, and delivery devices [56]. Recently, solid electrolyte entrapped piezo polymeric separators were developed by few researchers for direct applications in self-charging power (supercapacitor or battery) cells [57]. Herein, Raman spectral and mapping analysis are used to study the distribution of electrolyte ions inside the polymer matrix and also to understand the role of electrolyte ions on the self-poling properties to yield the electroactive phase in the PVDF [58]. The piezo-polymer electrolyte nanocomposite film was prepared via the method given in Section 2.5 which contains PTA electrolyte distributed in the PVDF matrix. Initial studies on the Raman spectrum of bare and electrolyte incorporated films showed the presence of α -phase (765 & 880 cm^{-1}) and electroactive β -phase (842 cm^{-1}) in the bare PVDF whereas the presence of band due to W-O stretching (1011 cm^{-1}) were found in the composite films [16]. The Raman spectral analysis of the piezo-electrolyte film shows that there were no changes found in the electroactive phases of PVDF due to the addition of PTA. Additionally, Raman mapping analysis is performed over an area of $-1 \times 1 \mu\text{m}^2$ with acquisition of 100 spectral arrays to study the distribution of the PTA in the PVDF polymer. **Figure 5(A)** depicts the 3D array map of PTA-PVDF revealing the presence of γ (811 cm^{-1}) and β (842 cm^{-1}) phase of PVDF and W-O vibrations (1011 cm^{-1}) of PTA electrolyte [16]. The peak position map of β -phase (**Figure 5(B)**) shows that their positions vary from 838 to 839 cm^{-1} (blue to red regime) whereas the position of the W-O vibration (**Figure 5(C)**) ranged from 1006.6 to 1007.5 (blue to red regime). **Figure 5(D)** and **(E)** presents the Raman intensity maps of β -phase PVDF (842 cm^{-1}) and (W-O 1011 cm^{-1}) respectively. The intensity ratio maps of $I_{\text{W-O}}/I_{\beta}$ (given in **Figure 5(F)**) shows that these values are in the range from 1.198 (blue) to 1.202 (red) indicating a high order of homogeneity [16]. There is no drastic variation in the intensity ratio from which it can be concluded that PTA electrolyte is homogeneously dispersed well in the PVDF matrix [16].

3.6 Raman spectroscopy as a tool to probe the mechanical to electrical energy transduction process in CEC film

The digital photographs of the bare PVDF and CEC film (**Figure 6(A)**) shows the transformation of white to black-colored films as a result of dehydrohalogenation process [59]. The predicted structures of linear carbyne chain present in the CEC film in horizontal and vertical orientation is provided in (**Figure 6(B)** and **(C)**). The 3D Raman array map of CEC film (**Figure 6(D)**) shows the presence of β -carbyne (cumulene) and carbonoid (sp , sp^2 , and sp^3 hybridized carbon) networks at 1140 and 1540 cm^{-1} , respectively [60]. The formation of sp^2 and sp^3 hybridized carbon can be explained via cross-linking reactions of adjacent sp -hybridized carbon in the carbyne chains during chemical reaction [22, 61]. The position map of the cumulene (**Figure 6(E)**) shows the width of about 40 cm^{-1} (blue to red-yellow color) as an indication of uniform distribution of ((=C=C=)_n) chains in the entire region of the CEC film. The carbonoid position map (**Figure 6(F)**) lies between 1525 and 1560 cm^{-1} (blue to red color) revealing the existence of sp -carbon in the mapped area. **Figure 6(G)** and **(H)** shows the intensity maps of cumulene and carbonoid bands of CEC. **Figure 6(I)** depicts the intensity-ratio map of cumulenic/carbonoid type carbon present in the CEC is in the range of 0.20 to 0.75, thus, confirmed the presence of uniformly distributed cumulene chains randomly oriented in the carbonoid species of the CEC [22].

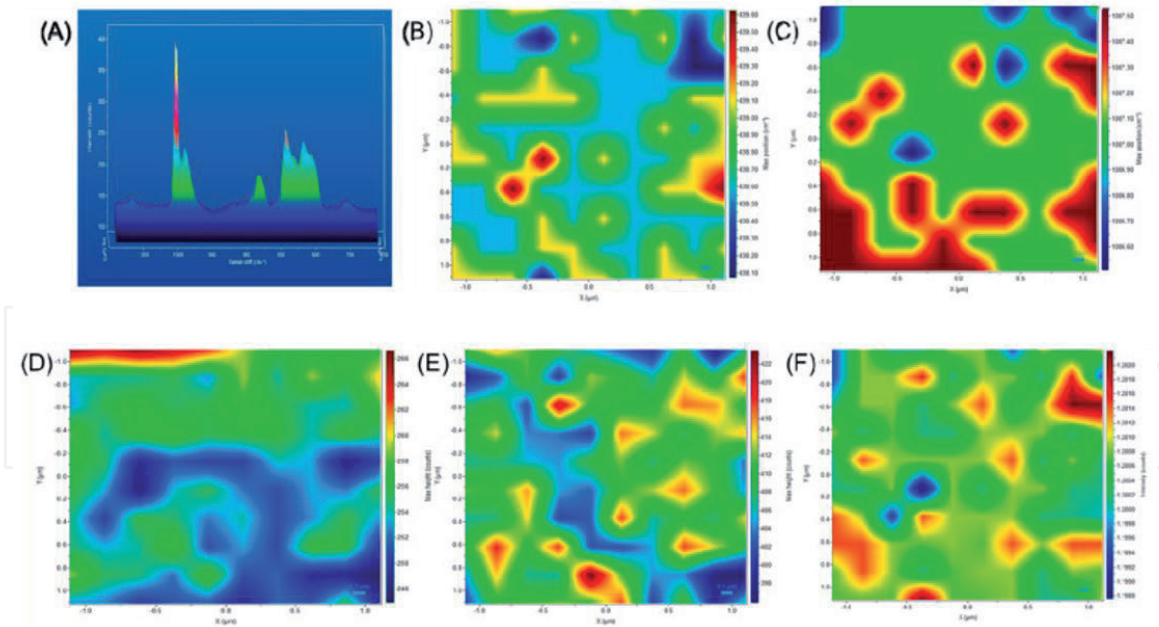


Figure 5. Raman characterization of the PTA-PVDF film. (A) 3D Raman array map, (B-C) peak position map of (B) β -PVDF (839 cm^{-1}) and (C) W-O band (1007 cm^{-1}), (D) β -PVDF band intensity map (E) W-O band intensity map, (F) I_{W-O}/I_{β} intensity ratio map.

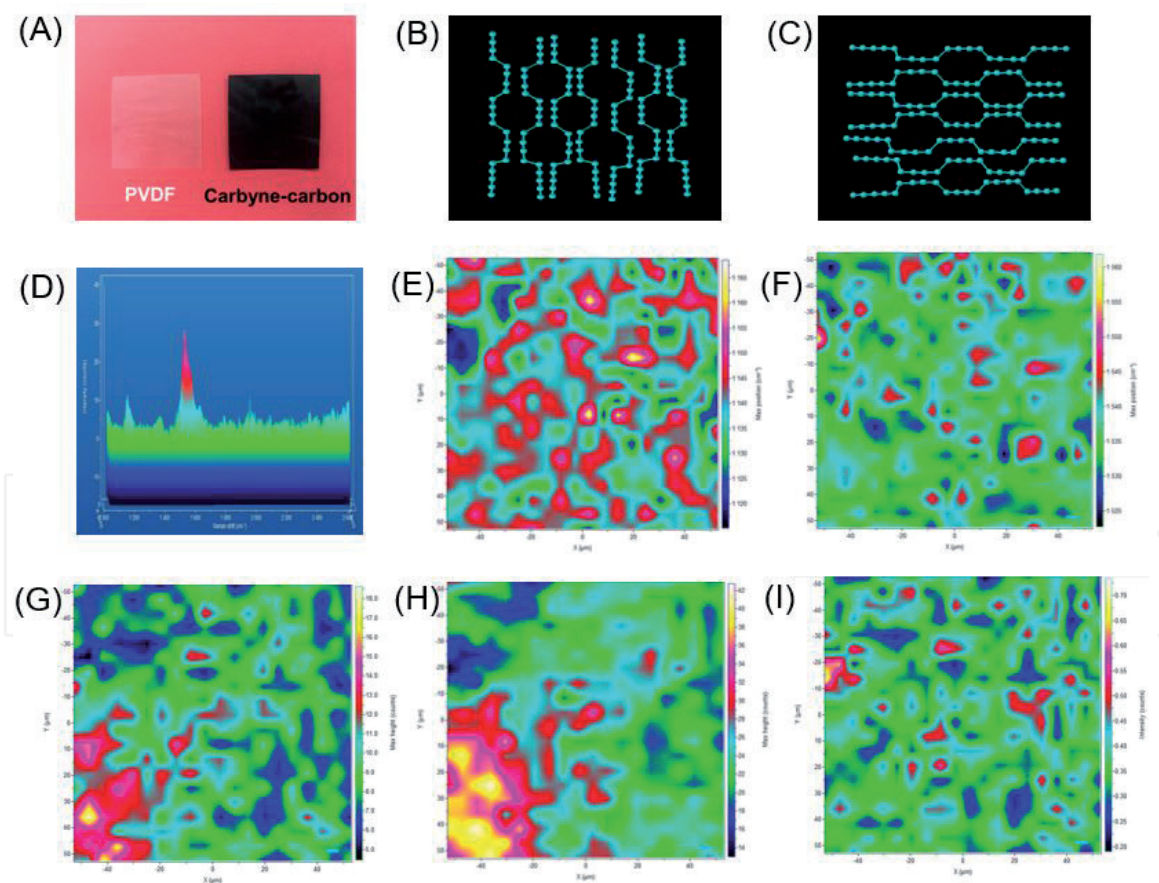


Figure 6. (A) Digital photograph of PVDF and CEC film, (B, C) structures of carbyne orientation in the horizontal and vertical orientation, (D) 3D Raman map of CEC film, (E) Cumulene peak-position map, (F) Carbonoids peak-position map, (G and H) represents the intensity maps of (G) cumulene and (H) carbonoid-carbon bands, and (I) integral intensity ratio map (I_{1140}/I_{1540}) of CEC.

Figure 7(A) and **(B)** summarizes the mechanical to electrical energy transduction properties of the CEC film when subjected to an applied force. The CEC film generates an electrical voltage and current outputs of $\sim 6.4\text{ V}$ and $\sim 10\text{ nA}$ while

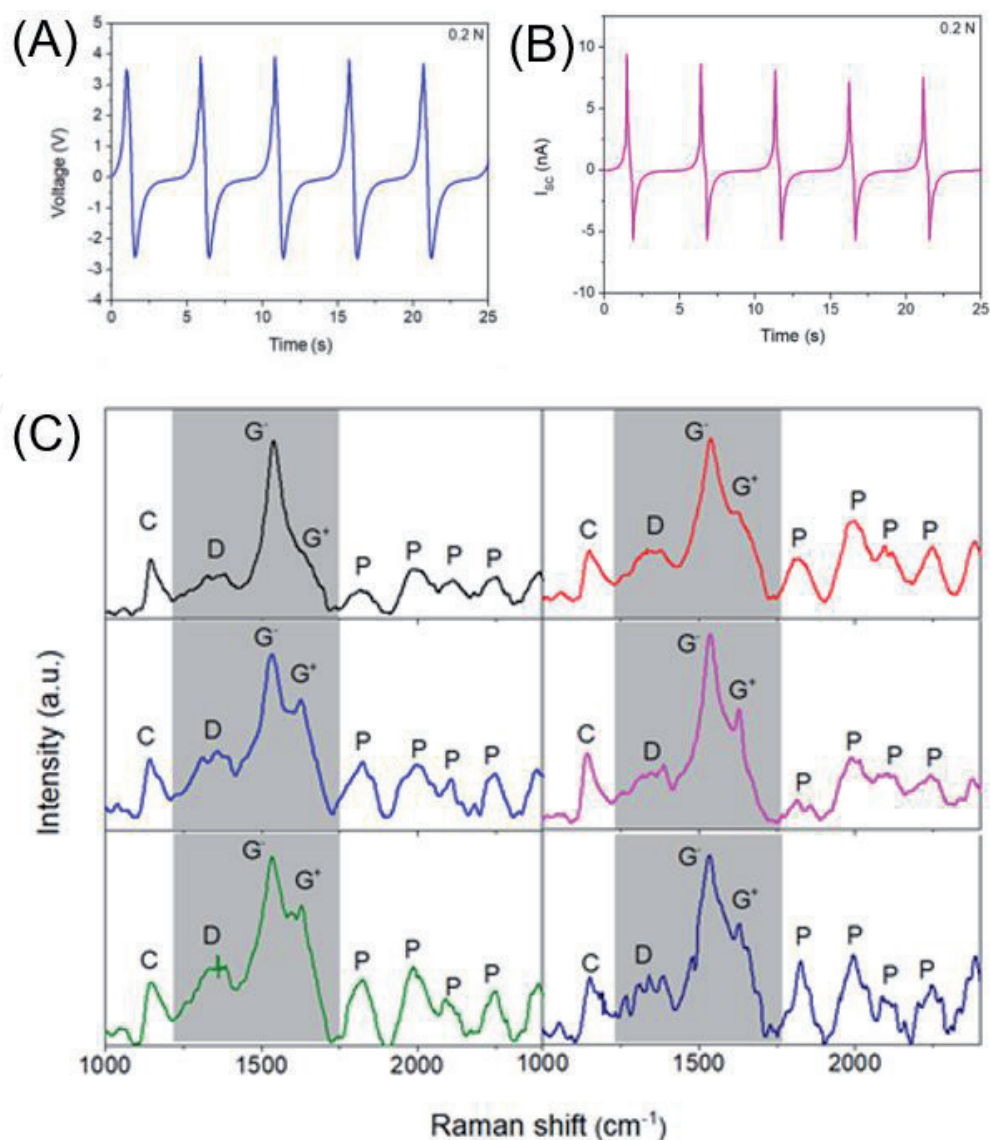


Figure 7. (A) Voltage and (B) current outputs of CEC film when subjected to 0.1 N force, (C) *ex-situ* Raman spectrum of CEC film recorded at various spots subjected to mechanical stimuli.

subjected to an external applied force of 0.2 N [22]. The electrical output ranges were increased linearly with respect to an increase in forces, demonstrating their ideal electromechanical stability [62]. The observation of mechanical to electrical energy harvesting properties in carbon-based materials are not new. For instance, these types of properties were observed earlier in graphene sheets, graphene oxides, lithiated carbon fibers, carbon nanotubes (CNT), twisting CNT yarn, and graphene nitrides very recently [63–66]. However, the mechanism of energy harvesting in these carbons are different to each other. Very recently, Raman spectroscopy is used to probe the presence of alkene/alkyne transition as a cause for the electrochemical actuation process involved in graphdiyne [67]. Considering the physical properties of carbynes that can be tuned upon subjected to any form of external stimuli, and the recent theoretical studies, it is possible that chemical bonding/structural transformation can be occurred in CEC when subjected to mechanical deformation. Therefore, *ex-situ* Raman spectral analysis of CEC (in deformed state) as shown in **Figure 7(C)** is analyzed to understand their detailed mechanism of energy transduction process. In comparison to the Raman spectrum of CEC film recorded at normal states, the *ex-situ* Raman analysis obtained at deformed state showed interesting observations as follows: (i) The cumulenic band is retained in the CEC even at deformed condition, (ii) the origin of D band ($\sim 1370 \text{ cm}^{-1}$) as a

result of deformation induced defects at the surface states [68, 69], (iii) occurrence of band splitting of the carbonoid band into G^- (1540 cm^{-1}) and G^+ (1590 cm^{-1}) bands due to origin of semiconducting behavior [68, 70], and (iv) the appearance of new bands over the region 1750 to 2300 cm^{-1} corresponding to the polynne type sp- carbon [71, 72]. These findings demonstrated the structural transformation of carbonoid type carbon in the CEC into semiconducting-type and polynne-type carbons via mechanical deformation which is the reason for the observed mechanical to electrical energy conversion in CEC. Moreover, these experimental results support the theoretical analysis on “electronic flexoelectricity” in low-dimensional carbon nanostructures subjected to mechanical deformation [73, 74].

4. Conclusions

This chapter describes the use of Raman spectroscopy and mapping analysis for the characterization for low-dimensional nanostructured materials, paint coatings, and solid electrolyte- piezo-polymer composites. Further, utilization of Raman spectroscopy to monitor the molecular level changes occurred in carbyne-enriched carbyne film based mechanical energy harvester when they are subjected to applied force is also described. Overall, this chapter provides a novel insight for the use of Raman spectroscopy and mapping as an important tool for characterization of low-dimensional nanostructures.

Acknowledgement

This research work was supported by the Basic Science Research Program through the National Research Foundation of Korea (NRF) grant funded by the Korean government (MSIT) (2019R1A2C3009747, 2020R1A2C2007366, and 2021R1A4A2000934).

Author details


Karthikeyan Krishnamoorthy^{1*} and Sang-Jae Kim^{1,2*}

¹ Nanomaterials and System Laboratory, Major of Mechatronics Engineering, Faculty of Applied Energy System, Jeju National University, Jeju, Republic of Korea

² R & D Center for New Energy Industry, Jeju National University, Jeju, Republic of Korea

*Address all correspondence to: karthi.nanotech@gmail.com and kimsangj@jejunu.ac.kr

IntechOpen

© 2021 The Author(s). Licensee IntechOpen. This chapter is distributed under the terms of the Creative Commons Attribution License (<http://creativecommons.org/licenses/by/3.0>), which permits unrestricted use, distribution, and reproduction in any medium, provided the original work is properly cited. 

References

- [1] A.M. Herrero, Raman spectroscopy a promising technique for quality assessment of meat and fish: A review, *Food Chem.* 107 (2008) 1642-1651. <https://doi.org/10.1016/j.foodchem.2007.10.014>.
- [2] M. Paillet, R. Parret, J.-L. Sauvajol, P. Colombari, Graphene and related 2D materials: An overview of the Raman studies, *J. Raman Spectrosc.* 49 (2018) 8-12. <https://doi.org/10.1002/jrs.5295>.
- [3] H. Zhou, C.S. Simmons, M. Sarntinoranont, G. Subhash, Raman Spectroscopy Methods to Characterize the Mechanical Response of Soft Biomaterials, *Biomacromolecules.* 21 (2020) 3485-3497. <https://doi.org/10.1021/acs.biomac.0c00818>.
- [4] B. Jalali, V. Raghunathan, D. Dimitropoulos, Ö. Boyraz, Raman-based silicon photonics, *IEEE J. Sel. Top. Quantum Electron.* 12 (2006) 412-421. <https://doi.org/10.1109/JSTQE.2006.872708>.
- [5] M. Dandu, K. Watanabe, T. Taniguchi, A.K. Sood, K. Majumdar, Spectrally Tunable, Large Raman Enhancement from Nonradiative Energy Transfer in the van der Waals Heterostructure, *ACS Photonics.* 7 (2020) 519-527. <https://doi.org/10.1021/acsp Photonics.9b01648>.
- [6] J. Ju, C.M. Hsieh, Y. Tian, J. Kang, R. Chia, H. Chang, Y. Bai, C. Xu, X. Wang, Q. Liu, Surface Enhanced Raman Spectroscopy Based Biosensor with a Microneedle Array for Minimally Invasive in Vivo Glucose Measurements, *ACS Sensors.* 5 (2020) 1777-1785. <https://doi.org/10.1021/acssensors.0c00444>.
- [7] X. Lin, Y. Wang, L. Wang, Y. Lu, J. Li, D. Lu, T. Zhou, Z. Huang, J. Huang, H. Huang, S. Qiu, R. Chen, D. Lin, S. Feng, Interference-free and high precision biosensor based on surface enhanced Raman spectroscopy integrated with surface molecularly imprinted polymer technology for tumor biomarker detection in human blood, *Biosens. Bioelectron.* 143 (2019) 111599. <https://doi.org/10.1016/j.bios.2019.111599>.
- [8] S. Gulyamov, M. Shamshiddinova, W. Bae, Y.C. Park, H.J. Kim, W. Cho, Y. Lee, Identification of biomarkers on kidney failure by Raman spectroscopy, *J. Raman Spectrosc.* (2021) jrs.6210. <https://doi.org/10.1002/jrs.6210>.
- [9] R.R. Jones, D.C. Hooper, L. Zhang, D. Wolverson, V.K. Valev, Raman Techniques: Fundamentals and Frontiers, *Nanoscale Res. Lett.* 14 (2019) 1-34. <https://doi.org/10.1186/s11671-019-3039-2>.
- [10] K.J.I. Ember, M.A. Hoeve, S.L. McAughtrie, M.S. Bergholt, B.J. Dwyer, M.M. Stevens, K. Faulds, S.J. Forbes, C.J. Campbell, Raman spectroscopy and regenerative medicine: a review, *Npj Regen. Med.* 2 (2017) 1-10. <https://doi.org/10.1038/s41536-017-0014-3>.
- [11] G.M. Do Nascimento, Introductory Chapter: The Multiple Applications of Raman Spectroscopy, in: *Raman Spectrosc.*, InTech, 2018. <https://doi.org/10.5772/intechopen.75795>.
- [12] G. Morari do Nascimento, Raman Spectroscopy and Imaging of Carbon Allotropes, in: *Mod. Spectrosc. Tech. Appl.*, IntechOpen, 2020. <https://doi.org/10.5772/intechopen.90867>.
- [13] X. Yu, Z. Zhang, F. Liu, Y. Ren, Synthesis of transfer-free graphene on cemented carbide surface, *Sci. Rep.* 8 (2018) 4759. <https://doi.org/10.1038/s41598-018-23206-8>.
- [14] F. Tres, K. Treacher, J. Booth, L.P. Hughes, S.A.C. Wren, J.W. Aylott, J.C. Burley, Real time Raman imaging to

- understand dissolution performance of amorphous solid dispersions, *J. Control. Release.* 188 (2014) 53-60. <https://doi.org/10.1016/j.jconrel.2014.05.061>.
- [15] K. Krishnamoorthy, M. Veerapandian, K. Yun, S.-J. Kim, The chemical and structural analysis of graphene oxide with different degrees of oxidation, *Carbon N. Y.* 53 (2013) 38-49. <https://doi.org/10.1016/j.carbon.2012.10.013>.
- [16] S. Manoharan, P. Pazhamalai, V.K. Mariappan, K. Murugesan, S. Subramanian, K. Krishnamoorthy, S.-J. Kim, Proton conducting solid electrolyte-piezoelectric PVDF hybrids: Novel bifunctional separator for self-charging supercapacitor power cell, *Nano Energy.* 83 (2021) 105753. <https://doi.org/10.1016/j.nanoen.2021.105753>.
- [17] K. Krishnamoorthy, P. Pazhamalai, J.H. Lim, K.H. Choi, S.-J. Kim, M.P. Pazhamalai, J.H. Lim, K.H. Choi, S.-J. Kim, Mechanochemical Reinforcement of Graphene Sheets into Alkyd Resin Matrix for the Development of Electrically Conductive Paints, *ChemNanoMat.* 4 (2018) 568-574. <https://doi.org/10.1002/cnma.201700391>.
- [18] K. Krishnamoorthy, G.K. Veerasubramani, P. Pazhamalai, S.J. Kim, Designing two dimensional nanoarchitected MoS₂ sheets grown on Mo foil as a binder free electrode for supercapacitors, *Electrochim. Acta.* 190 (2016) 305-312. <https://doi.org/10.1016/j.electacta.2015.12.148>.
- [19] K. Krishnamoorthy, P. Pazhamalai, S.-J.J. Kim, Two-dimensional siloxene nanosheets: novel high-performance supercapacitor electrode materials, *Energy Environ. Sci.* 11 (2018) 1595-1602. <https://doi.org/10.1039/C8EE00160J>.
- [20] V.K. Mariappan, K. Krishnamoorthy, P. Pazhamalai, S. Natarajan, S. Sahoo, S.S. Nardekar, S.-J. Kim, Antimonene dendritic nanostructures: Dual-functional material for high-performance energy storage and harvesting devices, *Nano Energy.* 77 (2020) 105248. <https://doi.org/10.1016/j.nanoen.2020.105248>.
- [21] V.K. Mariappan, K. Krishnamoorthy, P. Pazhamalai, S.-J. Kim, Exploring the bifunctional properties of paper-like carbyne-enriched carbon for maintenance-free self-powered systems, *Mater. Adv.* 1 (2020) 1644-1652. <https://doi.org/10.1039/D0MA00324G>.
- [22] K. Krishnamoorthy, V.K. Mariappan, P. Pazhamalai, S. Sahoo, S.-J. Kim, Mechanical energy harvesting properties of free-standing carbyne enriched carbon film derived from dehydrohalogenation of polyvinylidene fluoride, *Nano Energy.* 59 (2019) 453-463. <https://doi.org/10.1016/j.nanoen.2019.02.041>.
- [23] T. Yu, Z. Ni, C. Du, Y. You, Y. Wang, Z. Shen, Raman mapping investigation of graphene on transparent flexible substrate: The strain effect, *J. Phys. Chem. C.* 112 (2008) 12602-12605. <https://doi.org/10.1021/jp806045u>.
- [24] D.W. Lee, J.W. Seo, Sp²/Sp³ carbon ratio in graphite oxide with different preparation times, *J. Phys. Chem. C.* 115 (2011) 2705-2708. <https://doi.org/10.1021/jp107906u>.
- [25] U.K. Sur, Graphene: A Rising Star on the Horizon of Materials Science, *Int. J. Electrochem.* 2012 (2012) 1-12. <https://doi.org/10.1155/2012/237689>.
- [26] D. Chen, H. Feng, J. Li, Graphene oxide: Preparation, functionalization, and electrochemical applications, *Chem. Rev.* 112 (2012) 6027-6053. <https://doi.org/10.1021/cr300115g>.
- [27] A.C. Ferrari, J. Robertson, Interpretation of Raman spectra of

- disordered and amorphous carbon, *Phys. Rev. B.* 61 (2000) 14095-14107. <https://doi.org/10.1103/PhysRevB.61.14095>.
- [28] L.G. Cañado, K. Takai, T. Enoki, M. Endo, Y.A. Kim, H. Mizusaki, A. Jorio, L.N. Coelho, R. Magalhães-Paniago, M.A. Pimenta, General equation for the determination of the crystallite size l_a of nanographite by Raman spectroscopy, *Appl. Phys. Lett.* 88 (2006) 163106. <https://doi.org/10.1063/1.2196057>.
- [29] T. Wang, G. Chen, C. Wu, D. Wu, Study on the graphite nanosheets/resin shielding coatings, *Prog. Org. Coatings.* 59 (2007) 101-105. <https://doi.org/10.1016/j.porgcoat.2006.12.006>.
- [30] L.L. Vovchenko, L.Y. Matzui, V. V. Oliynyk, V.L. Launetz, The Effect of Filler Morphology and Distribution on Electrical and Shielding Properties of Graphite-Epoxy Composites, *Mol. Cryst. Liq. Cryst.* 535 (2011) 179-188. <https://doi.org/10.1080/15421406.2011.538335>.
- [31] S. Kataria, A. Patsha, S. Dhara, A.K. Tyagi, H.C. Barshilia, Raman imaging on high-quality graphene grown by hot-filament chemical vapor deposition, *J. Raman Spectrosc.* 43 (2012) 1864-1867. <https://doi.org/10.1002/jrs.4113>.
- [32] D. Graf, F. Molitor, K. Ensslin, C. Stampfer, A. Jungen, C. Hierold, L. Wirtz, Raman imaging of graphene, *Solid State Commun.* 143 (2007) 44-46. <https://doi.org/10.1016/j.ssc.2007.01.050>.
- [33] N. Islam, M.N.F. Hoque, W. Li, S. Wang, J. Warzywoda, Z. Fan, Vertically edge-oriented graphene on plasma pyrolyzed cellulose fibers and demonstration of kilohertz high-frequency filtering electrical double layer capacitors, *Carbon N. Y.* 141 (2019) 523-530. <https://doi.org/10.1016/j.carbon.2018.10.012>.
- [34] L. Wang, S. Li, F. Huang, X. Yu, M. Liu, H. Zhang, Interface modification of hierarchical $\text{Co}_9\text{S}_8@\text{NiCo}$ layered dihydroxide nanotube arrays using polypyrrole as charge transfer layer in flexible all-solid asymmetric supercapacitors, *J. Power Sources.* 439 (2019) 227103. <https://doi.org/10.1016/j.jpowsour.2019.227103>.
- [35] Y. Yao, L. Ren, S. Gao, S. Li, Histogram method for reliable thickness measurements of graphene films using atomic force microscopy (AFM), *J. Mater. Sci. Technol.* 33 (2017) 815-820. <https://doi.org/10.1016/j.jmst.2016.07.020>.
- [36] X. Li, H. Zhu, Two-dimensional MoS_2 : Properties, preparation, and applications, *J. Mater.* 1 (2015) 33-44. <https://doi.org/10.1016/j.jmat.2015.03.003>.
- [37] M. Acerce, D. Voiry, M. Chhowalla, Metallic 1T phase MoS_2 nanosheets as supercapacitor electrode materials, *Nat. Nanotechnol.* 10 (2015) 313-318. <https://doi.org/10.1038/nnano.2015.40>.
- [38] Z. Yin, H. Li, H. Li, L. Jiang, Y. Shi, Y. Sun, G. Lu, Q. Zhang, X. Chen, H. Zhang, Single-Layer MoS_2 Phototransistors, *ACS Nano.* 6 (2012) 74-80. <https://doi.org/10.1021/nn2024557>.
- [39] K. Krishnamoorthy, G.K. Veerasubramani, S. Radhakrishnan, S.J. Kim, Supercapacitive properties of hydrothermally synthesized sphere like MoS_2 nanostructures, *Mater. Res. Bull.* 50 (2014) 499-502. <https://doi.org/10.1016/j.materresbull.2013.11.019>.
- [40] Y. Cheng, K. Yao, Y. Yang, L. Li, Y. Yao, Q. Wang, X. Zhang, Y. Han, U. Schwingenschlögl, Van der Waals epitaxial growth of MoS_2 on SiO_2/Si by chemical vapor deposition, *RSC Adv.* 3 (2013) 17287. <https://doi.org/10.1039/c3ra42171f>.

- [41] B. Chakraborty, H.S.S.R. Matte, A.K. Sood, C.N.R. Rao, Layer-dependent resonant Raman scattering of a few layer MoS₂, *J. Raman Spectrosc.* 44 (2013) 92-96. <https://doi.org/10.1002/jrs.4147>.
- [42] P. Ares, J.J. Palacios, G. Abellán, J. Gómez-Herrero, F. Zamora, Recent Progress on Antimonene: A New Bidimensional Material, *Adv. Mater.* 30 (2018) 1703771. <https://doi.org/10.1002/adma.201703771>.
- [43] S. Zhang, Z. Yan, Y. Li, Z. Chen, H. Zeng, Atomically Thin Arsenene and Antimonene: Semimetal-Semiconductor and Indirect-Direct Band-Gap Transitions, *Angew. Chemie Int. Ed.* 54 (2015) 3112-3115. <https://doi.org/10.1002/anie.201411246>.
- [44] X. Wang, J. He, B. Zhou, Y. Zhang, J. Wu, R. Hu, L. Liu, J. Song, J. Qu, Bandgap-Tunable Preparation of Smooth and Large Two-Dimensional Antimonene, *Angew. Chemie Int. Ed.* 57 (2018) 8668-8673. <https://doi.org/10.1002/anie.201804886>.
- [45] J. Medina-Ramos, R.C. Pupillo, T.P. Keane, J.L. DiMaggio, J. Rosenthal, Efficient Conversion of CO₂ to CO Using Tin and Other Inexpensive and Easily Prepared Post-Transition Metal Catalysts, *J. Am. Chem. Soc.* 137 (2015) 5021-5027. <https://doi.org/10.1021/ja5121088>.
- [46] L. Liang, Y. Xu, Y. Li, H. Dong, M. Zhou, H. Zhao, U. Kaiser, Y. Lei, Facile synthesis of hierarchical fern leaf-like Sb and its application as an additive-free anode for fast reversible Na-ion storage, *J. Mater. Chem. A.* 5 (2017) 1749-1755. <https://doi.org/10.1039/C6TA10345F>.
- [47] Y. Shao, Z.-L. Liu, C. Cheng, X. Wu, H. Liu, C. Liu, J.-O. Wang, S.-Y. Zhu, Y.-Q. Wang, D.-X. Shi, K. Ibrahim, J.-T. Sun, Y.-L. Wang, H.-J. Gao, Epitaxial Growth of Flat Antimonene Monolayer: A New Honeycomb Analogue of Graphene, *Nano Lett.* 18 (2018) 2133-2139. <https://doi.org/10.1021/acs.nanolett.8b00429>.
- [48] M. Fortin-Deschênes, O. Waller, T.O. Menteş, A. Locatelli, S. Mukherjee, F. Genuzio, P.L. Levesque, A. Hébert, R. Martel, O. Moutanabbir, Synthesis of Antimonene on Germanium, *Nano Lett.* 17 (2017) 4970-4975. <https://doi.org/10.1021/acs.nanolett.7b02111>.
- [49] H. Nakano, M. Ishii, H. Nakamura, Preparation and structure of novel siloxene nanosheets., *Chem. Commun. (Camb).* 2 (2005) 2945-2947. <https://doi.org/10.1039/b500758e>.
- [50] P. Pazhamalai, K. Krishnamoorthy, S. Sahoo, V.K. Mariappan, S.-J. Kim, Understanding the Thermal Treatment Effect of Two-Dimensional Siloxene Sheets and the Origin of Superior Electrochemical Energy Storage Performances, *ACS Appl. Mater. Interfaces.* 11 (2019) 624-633. <https://doi.org/10.1021/acsami.8b15323>.
- [51] K. Xu, L. Ben, H. Li, X. Huang, Silicon-based nanosheets synthesized by a topochemical reaction for use as anodes for lithium ion batteries, *Nano Res.* 8 (2015) 2654-2662. <https://doi.org/10.1007/s12274-015-0772-4>.
- [52] S. Li, H. Wang, D. Li, X. Zhang, Y. Wang, J. Xie, J. Wang, Y. Tian, W. Ni, Y. Xie, Siloxene nanosheets: a metal-free semiconductor for water splitting, *J. Mater. Chem. A.* 4 (2016) 15841-15844. <https://doi.org/10.1039/C6TA07545B>.
- [53] H. Imagawa, N. Takahashi, T. Nonaka, Y. Kato, K. Nishikawa, H. Itahara, Synthesis of a calcium-bridged siloxene by a solid state reaction for optical and electrochemical properties, *J. Mater. Chem. A.* 3 (2015) 9411-9414. <https://doi.org/10.1039/C5TA00321K>.
- [54] R. Fu, K. Zhang, R.P. Zaccaria, H. Huang, Y. Xia, Z. Liu, Two-dimensional silicon suboxides nanostructures with Si

- nanodomains confined in amorphous SiO₂ derived from siloxene as high performance anode for Li-ion batteries, *Nano Energy*. 39 (2017) 546-553. <https://doi.org/10.1016/J.NANOEN.2017.07.040>.
- [55] H.D. Fuchs, M. Stutzmann, M.S. Brandt, M. Rosenbauer, J. Weber, A. Breitschwerdt, P. Deák, M. Cardona, Porous silicon and siloxene: Vibrational and structural properties, *Phys. Rev. B*. 48 (1993) 8172-8189. <https://doi.org/10.1103/PhysRevB.48.8172>.
- [56] P. Yao, H. Yu, Z. Ding, Y. Liu, J. Lu, M. Lavorgna, J. Wu, X. Liu, Review on Polymer-Based Composite Electrolytes for Lithium Batteries, *Front. Chem.* 7 (2019) 522. <https://doi.org/10.3389/fchem.2019.00522>.
- [57] H. He, Y. Fu, T. Zhao, X. Gao, L. Xing, Y. Zhang, X. Xue, All-solid-state flexible self-charging power cell basing on piezo-electrolyte for harvesting/storing body-motion energy and powering wearable electronics, *Nano Energy*. 39 (2017) 590-600. <https://doi.org/10.1016/J.NANOEN.2017.07.033>.
- [58] C. Xu, L. Zhang, Y. Xu, Z. Yin, Q. Chen, S. Ma, H. Zhang, R. Huang, C. Zhang, L. Jin, W. Yang, J. Lu, Filling the holes in piezopolymers with a solid electrolyte: a new paradigm of poling-free dynamic electrets for energy harvesting, *J. Mater. Chem. A*. 5 (2017) 189-200. <https://doi.org/10.1039/C6TA07297F>.
- [59] V. V. Korshak, Y.P. Kudryavtsev, Y. V. Korshak, S.E. Evsyukov, V. V. Khvostov, V.G. Babaev, M.B. Guseva, Formation of β -carbyne by dehydrohalogenation, *Die Makromol. Chemie, Rapid Commun.* 9 (1988) 135-140. <https://doi.org/10.1002/marc.1988.030090304>.
- [60] N.N. Mel'nik, D.Y. Korobov, O.S. Plyashechnik, V. V. Savranskii, Raman spectra of carbyne-fullerene structures, *Bull. Lebedev Phys. Inst.* 40 (2013) 187-190. <https://doi.org/10.3103/S1068335613070038>.
- [61] F. Cataldo, D. Capitani, Preparation and characterization of carbonaceous matter rich in diamond-like carbon and carbyne moieties, *Mater. Chem. Phys.* 59 (1999) 225-231. [https://doi.org/10.1016/S0254-0584\(99\)00055-3](https://doi.org/10.1016/S0254-0584(99)00055-3).
- [62] N. Muralidharan, M. Li, R.E. Carter, N. Galio, C.L. Pint, Ultralow Frequency Electrochemical-Mechanical Strain Energy Harvester Using 2D Black Phosphorus Nanosheets, *ACS Energy Lett.* 2 (2017) 1797-1803. <https://doi.org/10.1021/acsenerylett.7b00478>.
- [63] M.T. Ong, E.J. Reed, Engineered Piezoelectricity in Graphene, *ACS Nano*. 6 (2012) 1387-1394. <https://doi.org/10.1021/nn204198g>.
- [64] L. Liu, Y. Cheng, L. Zhu, S.-T. Lee, F. Liao, M. Shao, The Surface Polarized Graphene Oxide Quantum Dot Films for Flexible Nanogenerators, *Sci. Rep.* 6 (2016) 32943. <https://doi.org/10.1038/srep32943>.
- [65] E. Jacques, G. Lindbergh, D. Zenkert, S. Leijonmarck, M.H. Kjell, Piezo-Electrochemical Energy Harvesting with Lithium-Intercalating Carbon Fibers, *ACS Appl. Mater. Interfaces*. 7 (2015) 13898-13904. <https://doi.org/10.1021/acsami.5b02585>.
- [66] M. V Ilina, Y.F. Blinov, O.I. Ilin, N.N. Rudyk, O.A. Ageev, Piezoelectric effect in non-uniform strained carbon nanotubes, *IOP Conf. Ser. Mater. Sci. Eng.* 256 (2017) 012024. <https://doi.org/10.1088/1757-899X/256/1/012024>.
- [67] C. Lu, Y. Yang, J. Wang, R. Fu, X. Zhao, L. Zhao, Y. Ming, Y. Hu, H. Lin, X. Tao, Y. Li, W. Chen, High-performance graphdiyne-based electrochemical actuators, *Nat. Commun.* 9 (2018) 752. <https://doi.org/10.1038/s41467-018-03095-1>.

[68] S. Takabayashi, K. Okamoto, T. Nakatani, Influence of post-annealing on a diamondlike carbon film analyzed by Raman spectroscopy, *Surf. Interface Anal.* 50 (2018) 441-447. <https://doi.org/10.1002/sia.6387>.

[69] S. Thangavel, K. Krishnamoorthy, V. Krishnaswamy, N. Raju, S.J. Kim, G. Venugopal, Graphdiyne-ZnO Nanohybrids as an Advanced Photocatalytic Material, *J. Phys. Chem. C.* 119 (2015) 22057-22065. <https://doi.org/10.1021/acs.jpcc.5b06138>.

[70] H. Telg, M. Fouquet, J. Maultzsch, Y. Wu, B. Chandra, J. Hone, T.F. Heinz, C. Thomsen, G- and G+ in the Raman spectrum of isolated nanotube: a study on resonance conditions and lineshape, *Phys. Status Solidi.* 245 (2008) 2189-2192. <https://doi.org/10.1002/pssb.200879658>.

[71] J. Kastner, H. Kuzmany, L. Kavan, F.P. Dousek, J. Kuerti, Reductive Preparation of Carbyne with High Yield. An in Situ Raman Scattering Study, *Macromolecules.* 28 (1995) 344-353. <https://doi.org/10.1021/ma00105a048>.

[72] K. Akagi, M. Nishiguchi, H. Shirakawa, Y. Furukawa, I. Harada, One-dimensional conjugated carbyne - synthesis and properties, *Synth. Met.* 17 (1987) 557-562. [https://doi.org/10.1016/0379-6779\(87\)90798-3](https://doi.org/10.1016/0379-6779(87)90798-3).

[73] S. V. Kalinin, V. Meunier, Electronic flexoelectricity in low-dimensional systems, *Phys. Rev. B.* 77 (2008) 033403. <https://doi.org/10.1103/PhysRevB.77.033403>.

[74] A.G. Kvashnin, P.B. Sorokin, B.I. Yakobson, Flexoelectricity in Carbon Nanostructures: Nanotubes, Fullerenes, and Nanocones, *J. Phys. Chem. Lett.* 6 (2015) 2740-2744. <https://doi.org/10.1021/acs.jpcclett.5b01041>.